High-resolution computation predicts that low dissolved CO concentrations and CO gradients promote ethanol production at industrial-scale gas fermentation

Puiman, Lars; Benalcázar, Eduardo Almeida; Picioreanu, Cristian; Noorman, Henk J.; Haringa, Cees

DOI
10.1016/j.bej.2024.109330

Publication date
2024

Document Version
Final published version

Published in
Biochemical Engineering Journal

Biochemical Engineering Journal 207 (2024) 109330

Contents lists available at ScienceDirect

Biochemical Engineering Journal

journal homepage: www.elsevier.com/locate/bej

Regular article

High-resolution computation predicts that low dissolved CO concentrations and CO gradients promote ethanol production at industrial-scale gas fermentation

Lars Puiman [a], Eduardo Almeida Benalcázar [a], Cristian Picioreanu [b], Henk J. Noorman [a,c], Cees Haringa [a,*]

[a] Department of Biotechnology, Delft University of Technology, Delft, the Netherlands
[b] Biological and Environmental Sciences and Engineering Division, Water Desalination and Reuse Center, King Abdullah University of Science and Technology, Thuwal, Saudi Arabia
[c] dsm-firmenich, Delft, the Netherlands

ARTICLE INFO

Keywords:
Gas fermentation
Concentration gradients
CFD
Metabolic modelling
Lifelines
Industrial

ABSTRACT

Gradients in dissolved gas concentrations are expected to affect the performance of large reactors for anaerobic gas (CO, H_2, CO_2) fermentation. To study how these gradients, and the dissolved gas concentration level itself, influence the productivity of the desired product ethanol and the product spectrum of *C. autoethanogenum*, we coupled a CFD model of an industrial-scale gas fermentor to a metabolic kinetic model for a wide range of metabolic regimes. Our model results, together with literature experimental data and a model with constant dissolved gas concentrations, indicate high ethanol specificity at low dissolved CO concentrations, with acetate reduction to ethanol at very low dissolved CO concentrations and combined ethanol and acetate production at higher CO concentrations. The gradient was predicted to increase both the biomass-specific ethanol production rate and the electron-to-ethanol yield by ~25%. This might be due to intensified ferredoxin and NAD^+ redox cycles, with the rate of the Rnf complex – a critical enzyme for energy conservation – as key driver towards ethanol production, all at the expense of a reduced flux to acetate. We present improved mechanistic understanding of the gas fermentation process, and novel leads for optimization and fundamental research, by coupling observations from various down-scaled lab experiments to expected microbial lifelines in an industrial-scale reactor.

1. Introduction

In the last few years, anaerobic gas fermentation (with CO, H_2 and/or CO_2 gas mixtures) has successfully been commercialized by the company LanzaTech for the production of ethanol from industrial waste streams [1,2]. Ethanol is the product of main interest, since it has an established use as fuel and because it can be upgraded to plastics, textiles, and fine chemicals, while the spent microbial biomass can be used as animal feed [1–4]. The industrial gas fermentation process with the acetogen *Clostridium autoethanogenum* is deployed in external-loop gas-lift reactors (EL-GLR), which has shown potential for achieving high gas-to-liquid mass transfer rates, at least in part due the coalescence-inhibiting properties of the produced ethanol [5,6].

In large-scale bioreactors (e.g., the mentioned EL-GLR of ~500 m^3), gradients in (amongst others) liquid-phase substrate and dissolved gas concentrations are usually expected when the characteristic time of consumption is smaller than those of liquid circulation and mass transfer, respectively [7,8]. Moreover, variations in hydrostatic pressure and the gas composition were estimated to result in a gradient of factor 35 [9]. The temporal fluctuations that micro-organisms experience as a consequence of these spatial gradients (*lifelines*) were found to enlarge population heterogeneity [10–12], and often lead to reduced performance [13–15].

Recent works show that spatial dissolved gas concentration gradients are also expected in industrial-scale gas fermentation bioreactors, such

Abbreviations: CFD, computational fluid dynamics; CRD, cellular rection dynamics; EL-GLR, external-loop gas-lift reactor; VE, volume element.

* Correspondence to: Delft University of Technology, Faculty of Applied Sciences, Department of Biotechnology, Van der Maasweg 9, Delft 2629HZ, the Netherlands.
E-mail address: C.Haringa@tudelft.nl (C. Haringa).

https://doi.org/10.1016/j.bej.2024.109330
Received 25 January 2024; Received in revised form 8 April 2024; Accepted 9 April 2024
Available online 22 April 2024

List of symbols

Latin

c	Concentration (mol m^{-3} or g L^{-1})
J	Metabolic rate (mol mol_X^{-1} h^{-1})
k_La	volumetric mass transfer coefficient (h^{-1})
N_p	Number of particles for which the CRD model was solved
q	Biomass-specific rate (mol mol_X^{-1} h^{-1})
r	Volumetric rate (mol m_L^{-3} h^{-1})
$\tilde{r}_i$	Particle-specific rate (mol $particle^{-1}$ h^{-1})
t	Time (s)
Δt	Time step (s)
t_c	Circulation time (s)
t_m	95% mixing time (s)
V	Volume(m^{-3})

Greek

ε	Elasticity coefficient (-)
μ	Growth rate (h^{-1})
τ	Characteristic or turnover time (s^{-1})

Sub- and superscripts

0	Initial
EC	Extracellular
f	Flow
i	Compound
IC	Intracellular
j	Reaction
L	Liquid
ll	lin-log
p	Particle
ref	Reference
VE	Volume element
X	Biomass

as bubble columns [16,17] and the EL-GLR [9]. From the microbial perspective, the spatial concentration variations in the EL-GLR were predicted to result in frequent and irregular (5 – 30 s) cycles in dissolved gas (CO, H_2) concentrations with one order of magnitude [9]. Long periods (> 70 s) at low CO concentrations ($c_{L,CO}^{crit} < 0.003$ mol m^{-3}) were hypothesized to result into a starvation regime, with transcriptional changes as consequence, and reduced growth rates and product yields [16].

The impact of the concentration gradient on the cellular metabolic activity, and thus its product formation rate, can be studied by coupling a computational fluid dynamics (CFD) model of a bioreactor with a dynamic metabolic model (cellular reaction dynamics, CRD), in an Euler-Lagrangian computational framework. With a one-way coupled approach and kinetics applied to the Eulerian field, the impact of the concentration gradient on the microbial metabolism can relatively quickly be assessed, while with full Euler-Lagrangian two-way coupling the microbial metabolism also impacts the gradient. The first two-way coupled simulations for industrial fermentations were performed by Reuss and co-workers [12,18], after which follow-up work was done via various methodologies: Morchain et al. [19] used population balance models for microorganisms, while Haringa et al. [20] used a 9-pool dynamic kinetic model [21]. One-way coupled simulations for bubble column reactors were done for *Saccharomyces cerevisiae* [22] and *C. autoethanogenum* [9,16], and it was found that microorganisms in bubble columns typically experience shorter starvation periods than in stirred-tank reactors [23]. One of the major limitations of this approach is the computational power required for the high-resolution simulations, which can partially be relieved with the use of compartment models [24–26]. In recent years, the CFD-CRD modelling approach gained widespread attention, as it opens avenues towards more rational scale-up and optimization of industrial-scale bioreactors [27–29].

The metabolism of acetogens and the Wood-Ljungdahl pathway have extensively been described before [4,30,31]. Carbon (CO and CO_2) is fixed via the Wood-Ljungdahl pathway, which contains two branches: In the carbonyl branch CO is converted into CO_2 to reduce ferredoxins with the reversible carbon monoxide dehydrogenase (CODH) enzyme, while in the methyl branch CO_2 is converted into formate, which is further reduced to an activated methyl group. CO and the methyl group are then combined into acetyl-CoA at the expense of 1 ATP, which is recovered downstream through acetate production [31]. By the establishment of a chemiosmotic gradient, ATP for growth and maintenance is produced: The Rnf complex exports protons via electron transfer from reduced ferredoxin (Fd_{red}^{2-}) to NAD^+ [30,32]. Ethanol is mainly produced via the AOR pathway (named after the enzyme acetaldehyde:ferredoxin oxidoreductase), which is thermodynamically feasible only when the intracellular acetate concentration passed the threshold of 1000 times the acetaldehyde level [33,34]. High intracellular acetate concentrations are obtained at low extracellular pH (5.0) and high concentrations of undissociated acetic acid, since this neutral form of the acid can passively diffuse into the cell [34]. H_2 uptake relates to ethanol production, as its electrons are directly stored in Fd_{red}^{2-} and NADPH [35,36].

A 12-pool CRD model was recently developed that could describe metabolic dynamics upon metabolic-induced self-oscillations [37] of *C. autoethanogenum* in a chemostat culture [38]. This model could explain how extracellular concentrations (of CO, H_2, CO_2, protons and the products acetic acid, ethanol and 2,3-butanediol), and the intracellular carbon (formate, acetyl-CoA, acetate) and electron pools (Fd_{red}^{2-}, NADH, NADPH), change upon fluctuations in any of these. From the self-oscillating culture, it was found that the biomass-specific ethanol production rate, q_{EtOH}, varies proportionally to the uptake rate of the electron donors (CO and H_2) [38]. By varying the redox potential among several batch cultures Grimalt-Alemany et al. (2021) observed severe dynamics (within one order of magnitude) in the NAD(H) pool size and the NADH/NAD^+ ratio, and that dynamics in the latter positively correlated with the ethanol specificity.

Since the observed dynamics in both studies (in the order of days) are of metabolic origin (no proteomic differences were observed in [37]) and related to thermodynamics, they may help identify how the short-timescale dynamics occurring in the industrial-scale bioreactor (in the order of seconds) affect the metabolism. Based on the dynamics in these experimental studies, we hypothesize that the temporal-variations in dissolved gas concentration as occurring in the industrial-scale EL-GLR, lead to increased q_{EtOH}, compared to a spatially- and temporally homogenous environment.

In this work, we coupled the CRD model [38] with our previously developed CFD model of an industrial-scale EL-GLR [5,9] supplied with a gas mix containing 50% CO, 20% H_2 and 30% CO_2, to study how the dissolved gas concentration and its gradient may influence the metabolic behaviour of *C. autoethanogenum* (with focus on the product spectrum, substrate inhibition, and energy conservation mechanisms). Computations were done with several biomass concentrations to study a wide range of fluctuations on dissolved gas concentrations, from conditions with excess mass transfer to severe mass transfer limitations (from over-reduced to significantly under-reduced conditions). By comparing the CFD-CRD model results with those of a model with constant dissolved gas concentrations, the impact of the dissolved gas concentration and its dynamics on the metabolism and product spectrum of *C. autoethanogenum* could be studied. From the results, we could

identify which metabolite pools, reactions and enzymes relate to ethanol production, establish several hypotheses for further research, and propose ways for reactor, strain and process optimization.

2. Methodology

2.1. CFD-CRD coupling approach

The CFD model (geometry, flow pattern and operation conditions) of an external-loop gas-lift reactor (~500 m^3) that was developed in our previous study [5], was complemented with a mass transfer model in [9], and, in the present work, with the CRD model developed in [38]. The hydrodynamic model was validated on pilot-scale data, while mass transfer rates of the EL-GLR corresponded with industrial standards by assuming bubbles with a constant diameter of 3 mm [5], possible due to coalescence inhibition [6]. The resulting Eulerian flow and concentration fields of the CFD simulation with black-box kinetics (with 5 $g_x\ L^{-1}$) and gas-liquid mass transfer, described in [9], was used as an initial condition for the CFD-CRD model described here. 250,000 Lagrangian particles were released at $t = 3000$ s, and mixed for 200 s, to ensure a homogeneous distribution of particles in the reactor at the start of the CFD-CRD simulation. The pH was kept constant at 5.0, while the initial external product and intracellular metabolite and co-factor concentrations were in the range of the ones used for the CRD model calibration [37,38] (Table A.1).

As soon as the CRD model was activated, two-way reaction coupling was applied for CO, H_2 and CO_2 according to the method described in [40,41], so that the metabolic-kinetic model determines the concentration fields and the gas hold-up. The basis for this two-way coupling procedure was described in [40]. A schematic overview of the model structure and its solving procedure is provided (Fig. 1).

The development and parameterization of the metabolic kinetic model are described extensively in [38] and the relevant parts for two-way coupling in SI A.1. The MATLAB model, comprising 12 metabolite pools and 12 reactions, was rewritten into C code, and implemented in an Euler-Lagrangian framework using the DPM_SCALAR_UPDATE macro in Ansys FLUENT. This allowed tracking and updating of particle-associated variables, specifically the metabolite concentrations, at every particle time step Δt_p, that was equal or smaller than the flow time step ($\Delta t_p \leq \Delta t_f = 5$ ms).

Since NADH has the lowest turnover time (~ 1 ms) the metabolic equations were integrated with a fixed – intracellular –time step Δt_{IC} of 0.1 ms. As $\Delta t_{IC} << \Delta t_p$, an integration routine was implemented using the Runge-Kutta 4th order algorithm. After each Δt_{IC}, the concentration vector was updated until Δt_p was completed. The particle position was updated, while the CRD model was integrated again, until the Eulerian time step Δt_f had been completed. At $t + \Delta t_p$, the volumetric source terms for CO, H_2, and CO_2 were computed for each particle within each volume element (VE) during the time step $\tilde{r}_i(p, \Delta t_p)$ using the concentration differences in that particle (Eq. 1). It was assumed that the amount of Lagrangian particles for which the CRD model was solved, N_p, are evenly distributed in the EL-GLR and that each particle equally

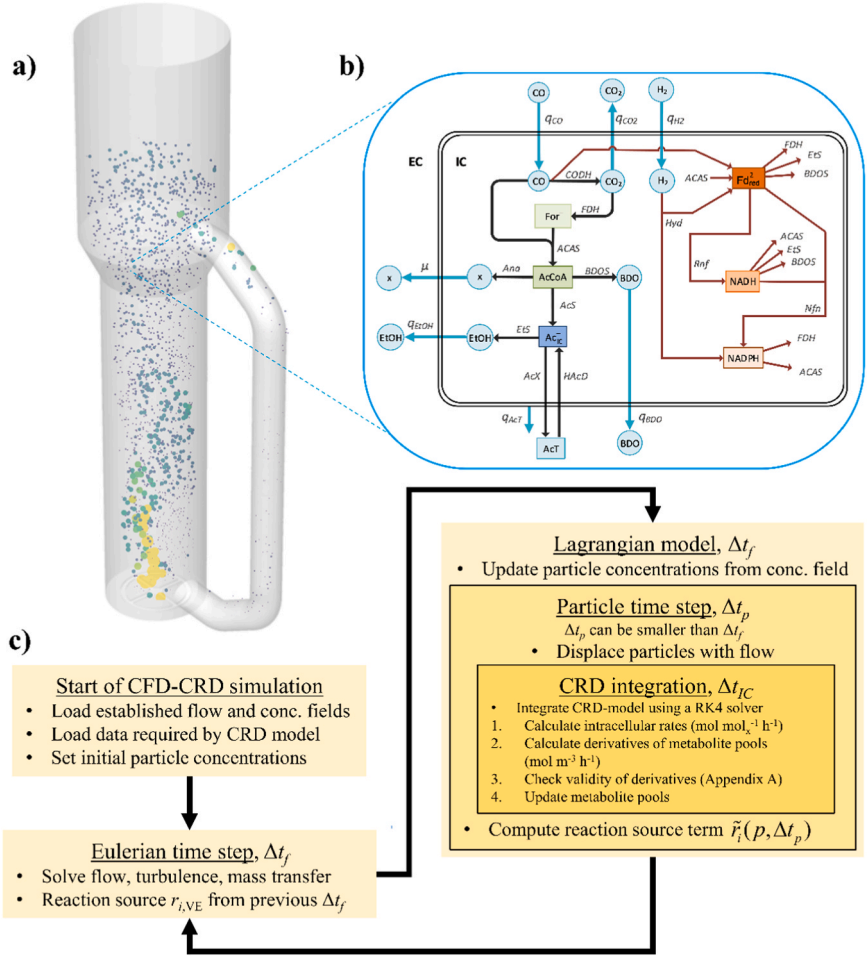

Fig. 1. Overview of the CFD-CRD model and its solving procedure. a) Geometry of the EL-GLR wherein the equations for flow, turbulence and mass transfer are solved, together with the displacement of Lagrangian particles. b) Structure of the metabolic-kinetic model, taken from [38]. c) Stepwise solving procedure of the CFD-CRD model implemented.

contributes to the total biomass concentration. After Δt_f the volumetric source terms for the dissolved species mass balances $r_{i,\mathrm{VE}}$ were computed per volume element by summation of $\widetilde{r}_i(p,\Delta t_p)$ over each particle and the number of Δt_p required to reach Δt_f.

$$r_{i,\mathrm{VE}} = \frac{\sum_{p=1}^{N_{p,\mathrm{VE}}} \sum_{\Delta t_p}^{\Delta t_f} \widetilde{r}_i(p,\Delta t_p)}{V_{L,\mathrm{VE}}} \text{ with } \widetilde{r}_i(p,\Delta t_p) = \frac{c_i|_{t+\Delta t_p} - c_i|_t}{\Delta t_p} \frac{V_{L,\mathrm{reactor}}}{N_p} \quad (1)$$

The metabolic model is based on lin-log kinetics, which is a good approximation of typical hyperbolic kinetics close to a given reference state [42,43], but leads to inaccurate and unstable behaviour in extreme regions [43,44]. Thus, results obtained with lin-log based metabolic models are most accurate within a rather narrow range of concentrations (typically one order of magnitude around the reference state). Such behaviour could therefore be expected when the CRD model is solved outside its range of calibration, for example at very low dissolved gas concentrations ($c_{\mathrm{L,CO}} < 0.025$ mol m^{-3}). As wide concentration ranges occur in the large-scale reactor, several modifications have been made to the solving procedure of the metabolic-kinetic model to increase solution stability (SI A.2). This comprises rate reversibility and a rate limitation mechanism based on a given set of minimum concentrations, preventing unrealistic rates and negative intracellular concentrations.

2.2. Model convergence and solution

During Δt_p the metabolite concentrations get updated, while the mass balances of the extracellular gas species only get updated after solving one flow time step Δt_f. As we assumed $c_{i,\mathrm{IC}} = c_{i,\mathrm{EC}}$ for the gases, their extracellular concentrations should be updated as often as possible to preserve the mass balances, requiring very short Δt_f. This implies that the integrated gas uptake rate of a particle during Δt_p, $r_{i,p} = \frac{c_i|_{t+\Delta t_p} - c_i|_t}{\Delta t_p}$, should be equal to the derivative at the beginning of that time step, $r_{i,p} = \left.\frac{dc_i}{dt}\right|_t$ (Equations A.3-A.6). As the flow time step directly affects the total simulation duration, we set Δt_f to 5 ms, a compromise between simulation accuracy and computational efficiency; N_p was fixed at 80,000 on similar grounds (SI A.5, Figures A.3, A.4).

The CFD-CRD model was solved for 1000 s flow time using Ansys Fluent 2021R2 for three biomass concentration cases, with c_x of 100, 150 and 200 mol m^{-3} (2.5, 3.75 and 5 g L^{-1}). Computations were done using the Snellius supercomputer with 128 cores of AMD Rome 7H12 CPU's, with an estimated simulation duration of 530 h per case.

Carbon and electron balance closure (relative error < 5%) for the lifelines were checked for model verification after completion of the CFD-CRD simulations. This was done for *i)* the original, unmodified ("raw"), CRD model (model α), *ii)* the CRD model with rate-limiting modifications (model β), and *iii)* by not considering the values obtained for $c_{\mathrm{L,CO}} < 0.025$ mol m^{-3} (model γ).

2.3. Post-processing

The following data was exported from FLUENT every 75 ms: the concentrations of each metabolite pool, the q_i of CO, H_2, CO_2, acetate and ethanol, and the position and the local number of particles $N_{p,\mathrm{VE}}$ were written (for 4000 particles, to prevent excessive data transport and storage). With this data, concentration profiles, derivatives and rates could be reconstructed by solving the CRD model for each moment in time in MATLAB, this approach was checked by additionally writing the derivatives for 20 particles. Lifeline data was analysed after removing the first 100 s (approximately one 95% mixing time). For visualization, the data was smoothed using MATLAB's smoothdata function, according to the moving mean algorithm with smoothing factor of 0.05.

Average particle metabolite concentrations and their derivatives were stored in every volume element, according to a rolling-average routine. The number of particles that was present in each volume element was registered and used to calculate the rolling average of these variables.

2.4. Model with constant concentrations

In order to determine the actual influence of the concentration gradients in the CFD-CRD model, the CRD model was also solved at constant dissolved gas concentrations. This was done for a wide range of fixed dissolved CO and H_2 concentrations. The CO concentration range was determined from the lifeline averages for each c_x, while the $c_{\mathrm{L,H2}}$ was found to be correlated to $c_{\mathrm{L,CO}}$ and determined via linear regression (Figure B.1); the CO_2 concentration was kept constant (Table B.1). The model was integrated with the same Runge-Kutta scheme as the CFD-CRD model, resetting the dissolved gas concentrations after each Δt_{IC} of 0.1 ms. The CRD model was solved for an interval of 1000 s (~1.5 min/simulation). This duration of 1000 s was chosen to be comparable with the CFD-CRD simulations, even if after this time the metabolism does not reach steady state.

3. Results and discussion

The results of our modelling study are presented first in terms of mass- and electron balances, to check the influence of the model modifications (Section 3.1). We look into the global reactor performance, in Section 3.2.–3.4, by analysing energy conservation, characteristic times and averages of individual lifelines. Then in Section 3.5, we zoom in to discuss the metabolic behaviour and the role of key cellular reactions (particularly the Rnf complex). Several hypotheses that emerged from the study are discussed in Section 3.6, while in the last section, 3.7, practical recommendations are provided for further optimizing gas fermentors.

3.1. Mass balances in the biomass phase

After solving the CFD-CRD model, we examined mass- and electron balance closure for various model modifications (Fig. 2). This analysis reveals that the electron balance never closed for the unmodified CRD model (α), with gaps of 10–20%. Implementation of the rate-limiting mechanism (model β) damped excessive rates (most prominently in J_{FDH}, J_{CODH}, J_{EtS} and J_{Rnf}). The mechanism ensured mass balance closure (within 5%) and resulted in a substantial reduction in q_{EtOH} from 0.4 mol $\mathrm{mol_x^{-1}h^{-1}}$ to a more realistic 0.15 mol $\mathrm{mol_x^{-1}h^{-1}}$.

The lin-log structure of the CRD model induced a numerical depletion of formate, at concentrations outside the range of calibration (Figure SI A.5). The rate-limiting mechanism dampens the formate depletion (cf., model α with β), although it could not entirely be avoided, due to the high minimum concentration that was required to solve the formate pool (10^{-4} vs. $<10^{-8}$ mol m^{-3} for other metabolites). As the rate-limiting modifications were only activated at low $c_{\mathrm{L,CO}}$, the numerically generated formate escalated ethanol production rates (q_{EtOH} increased from 0.09 to 0.15 mol $\mathrm{mol_x^{-1}h^{-1}}$, cf., β and γ). This results in uncertainty in the model predictions in the low CO concentration range. As both direct CO_2 reduction to formate ($CO_2 + H_2 \rightarrow For^- + H^+$) [45], and a formic acid import and formate export mechanism were not included in the CRD model, and as net CO_2 consumption was never observed, inclusion of these reactions in future work could improve the physical reliability of the model at lower $c_{\mathrm{L,CO}}$.

Irrespective of the used model, clear trends in the rates were observed: for example, at increased c_x higher q_{EtOH} was observed at the expense of acetate production (Ac^-_{IC} + AcT), while this was partly due to extracellular acetate consumption at increased c_x. As substantial parts of the reactor are operated under low CO conditions, removal or modification of these values from the lifelines would severely affect the magnitude and interpretation of the lifeline results. We hence proceed with model β in further analyses, considering the uncertainty in the

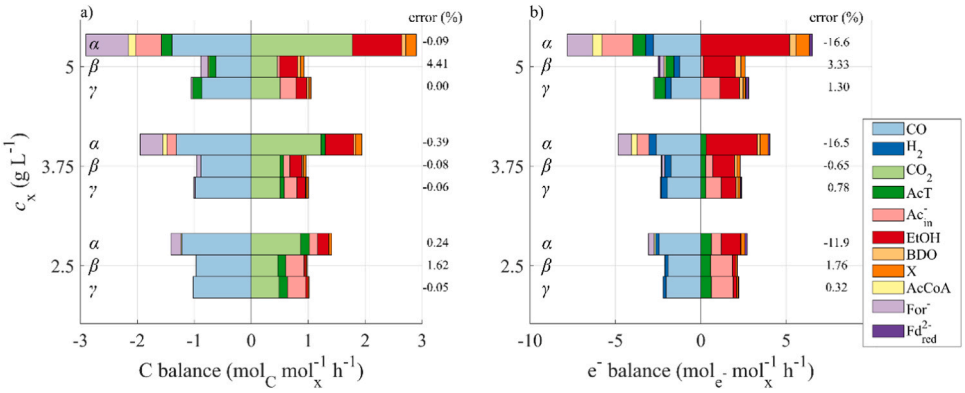

Fig. 2. Influence of the CRD model choice on the balances (denoted via metabolic rates) of post-processed lifelines. The a) carbon and b) electron mass balances are provided for the three c_x cases with the α: unmodified CRD model; β: CRD model with rate-limiting modifications; γ: model β applied for $c_{L,CO} > 0.025$ mol m^{-3}. These low $c_{L,CO}$ occurred in all c_x cases (62% of data at 5 g L^{-1} < 0.025 mol m^{-3}, 29% at 3.75 g L^{-1}and 10% with 2.5 g L^{-1}. Metabolic rates (colouring in legend) were averaged for 4000 lifelines during 900 s and balanced according to their respective carbon and electron contents. The relative mass balance error was calculated via the difference between the sum of positive and negative rates (as %).

model results at low CO concentrations.

3.2. Spatial distribution of energy conservation

In line with the gas hold-up profile in the EL-GLR, there is a clear spatial gradient in dissolved CO concentration, $c_{L,CO}$, of around one order of magnitude between the high and low concentration zones (Fig. 3a, b). Similar ε_G and $c_{L,CO}$ distributions were obtained in our previous study with Haldane-type CO uptake kinetics [9], indicating that such simulation results are largely insensitive to the model choice. High $c_{L,CO}$ is observed in locations with high ε_G, such as in the gas plume that is being pushed towards the left side due to the liquid flow exiting the downcomer, and in the gas plume that tends to converge towards the middle of the column. A small $c_{L,CO}$ pocket is present in the downcomer, due to some gas accumulation. The $c_{L,CO}$ we derived is still significantly higher than the ones reported in [16] due to the severe mass transfer limitations that were adopted in their simulations ($k_La \approx 40$ h^{-1}, here 360 h^{-1}). q_{CO} follows $c_{L,CO}$ (Fig. 3b, c) since uptake inhibition related to $c_{L,CO}$ was not predicted by the CRD model (see Sections 3.4 and 3.5).

Near the sparger, with locally high $c_{L,CO}$ and q_{CO}, high rates of ferredoxin reduction are observed (Fig. 3d). This indicates that our model predicts fast uptake (by diffusion) and utilization of the inflowing CO by CODH, and thus rapidly varying ferredoxin reduction rates, as was hypothesized [46] and measured before [47]. Higher up in the riser, $c_{L,CO}$ and q_{CO} are still high, but moderate reduction and oxidation rates are observed since the cells might be saturated with Fd^{2-}_{red}. At zones with low $c_{L,CO}$ and q_{CO} (downcomer, in the riser near the downcomer outlet, and close to the walls near the top separator), high re-oxidation rates of ferredoxin are observed. As soon as Fd^{2-}_{red} is oxidised, NAD^+ is reduced and ethanol is produced (Fig. 3e, f). The model predicts an inverse relationship between the ferredoxin redox state and the ethanol production rate; in zones where ferredoxin is reduced, little ethanol is produced, while ethanol is produced in zones where ferredoxin is oxidised. As a consequence, ethanol is mainly produced in zones with low gas hold-up and $c_{L,CO}$ (cf. Fig. 3b, e). From a microbial point of view, faster variations in dissolved gas concentration are expected to lead to faster ferredoxin oxidation/reduction cycles, and increased variations in q_{EtOH}.

Our model predicts via correlation analysis of lifeline data a significant delay (at least 15 s, with 5 and 3.75 g_x L^{-1}, and even 30 s with 2.5 g_x L^{-1}) between CO consumption and ethanol production, governed by the dissolved gas concentration gradient: only when $c_{L,CO}$ (and $c_{Fd^{2-}_{red}}$, Section 3.5) decrease, q_{EtOH} increases. This lag time is slightly shorter (~25%) than the circulation time, indicating that ethanol is being produced in a rather short period within the circulation. This is in sharp contrast with results from black-box and genome-scale metabolic models (using dFBA simulations), which both assume metabolic steady-state and show high production rates at locations with high gas uptake rates [48]. In our case the reactor can be subdivided in two zones: (1) a ferredoxin reduction zone and (2) a re-oxidation zone. Video S1 clearly shows the consequential differences in ethanol production zones compared to the black-box model. While further research is required to confirm these predictions, the model suggests a process design and operation that produces multiple, but smaller, of these zones, leading to shorter redox cycles, and improved ethanol productivity.

3.3. Analysis of characteristic times

Estimation of characteristic and turnover times is a widely used method for quick assessment of reactor performance and identification of limiting processes [7,8,49]. From the CFD-CRD model of the EL-GLR becomes clear that mixing and mass transfer are equally slow and generally slower (i.e., higher characteristic time) than CO uptake (Fig. 4), indicating that a dissolved CO gradient exist (in the cases with 3.75 and 5 g_x L^{-1}), which was confirmed in Fig. 3b. H_2 uptake is significantly slower than CO uptake, and its high characteristic time is expected to lead to a spatially well-distributed $c_{L,H2}$. The slow H_2 uptake mechanism was expected from experiments [35], as H_2 is thermodynamically the less preferred electron source in a gas mixture [50], and the cell can generate more ATP and reducing equivalents (Fd^{2-}_{red}, NADH, NADPH) per electron from CO than H_2 [51]. The H_2 uptake rates predicted with the CFD-CRD model are significantly lower than the ones that were predicted with the Monod kinetics used in our previous study (see SI C), indicating differences between models on the kinetic behaviour of H_2 uptake.

The model predicts that electron storage is done mainly via the ferredoxin pool. The Fd^{2-}_{red} pool has a similar turnover time compared to CO uptake, especially in the transport limited regime with 5 g_x L^{-1}. The turnover times mainly depend on the concentrations of the metabolite pools, causing that NADH and NADPH show a 100 and 10 time lower turnover time, respectively, which indicate even faster redox cycles of NAD^+ and $NADP^+$. The ferredoxin can thus be hypothesized as an electron buffer for the cell. As the intracellular concentration of Fd^{2-}_{red} was never measured, this hypothesis remains to be verified, although low concentrations of NADH and NADPH have indeed been measured before [37].

Similarly, the turnover time of acetate is high, while the other intermediates in the Wood-Ljungdahl pathway (formate and acetyl-CoA) are depleted significantly faster, in the cases with higher c_x. This shows a relatively fast pathway from acetyl-CoA to acetate production,

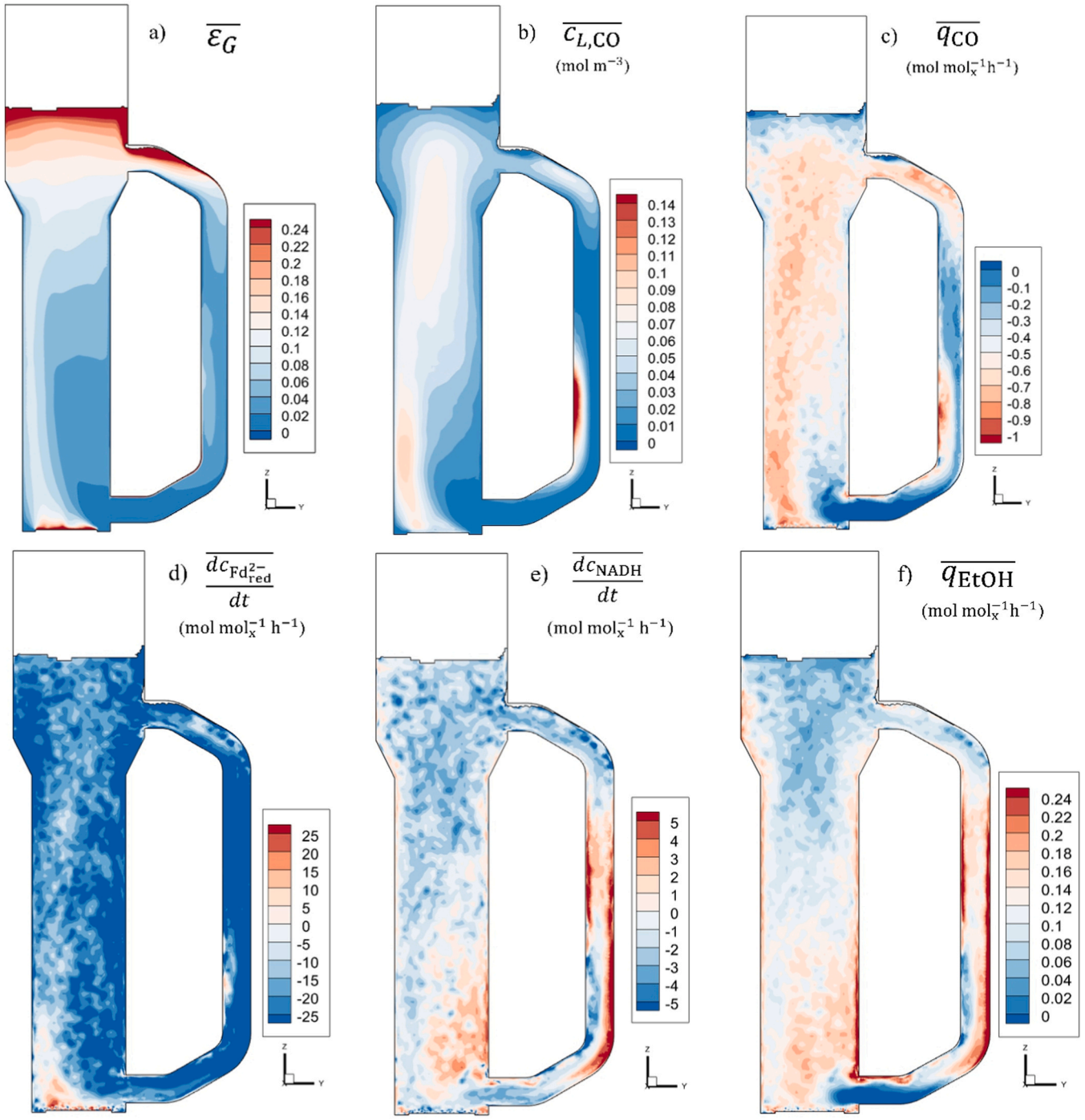

Fig. 3. Spatial variations in gas hold-up and metabolites in the EL-GLR. Surface plots in the *zy*-plane (x=0) of the EL-GLR with time-averaged a) ε_G, b) $c_{L,CO}$, c) q_{CO}, d, e) ferredoxin and NADH reduction rates (red) and oxidation rates (blue) respectively, f) q_{EtOH}. The results are time-averaged during the whole simulation duration of 1000 s, with $c_x = 5$ g L^{-1}.

despite the high concentrations of intracellular acetate due to the low pH (5.0) and the high extracellular concentration of acetic acid (90 mol m^{-3}). An interesting observation is the high formate turnover time: In the case with 2.5 g_x L^{-1}, large amounts of formate are over-produced at highly reduced conditions (with very high $c_{Fd^{2-}_{red}}$, and correspondingly at high $c_{L,CO}$) (Figure D.1). Formate production has been observed experimentally to relate with pressure [53,54], or with very low biomass concentrations [55], both resulting into very high $c_{L,CO}$.

The fast turnover time of CO suggests that the two-way coupling is not needed for the prediction of the $c_{L,CO}$ gradient, since a one-way coupling routine (with the Haldane kinetics) could also predict a similar gradient and lifelines. The CO and H_2 uptake rate in the CRD model are, however, predicted by considering the intracellular concentrations, which could lead to an inhibition effect (see Section 3.5). In order to account for such effects, implementation of a two-way coupling strategy is required.

3.4. Influence of dissolved CO on product spectrum

To study the influence of the concentration gradient on the global reactor performance, the results from the CFD-CRD simulations, based

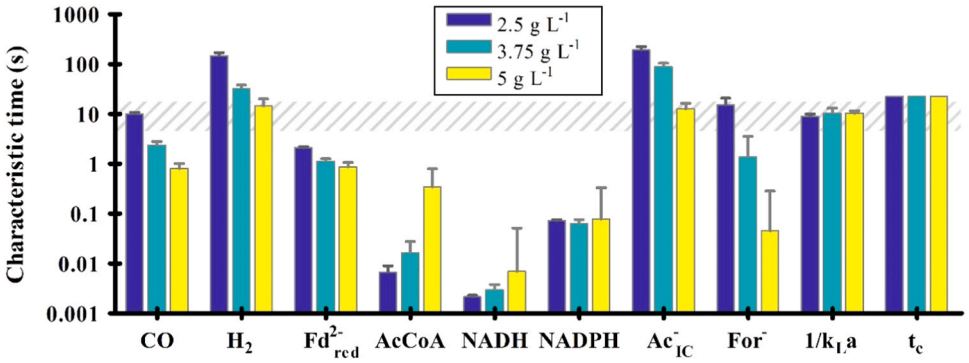

Fig. 4. Characteristic times for metabolite consumption, mass transfer and mixing. A spatial gradient may be present when the characteristic times are below the dashed grey zone, representing transport limitations. Turnover times of the metabolite pools were computed as the median of the ratio of the metabolite pool size and its depletion rate for 4000 lifelines ($\tau_i = c_i/J_i$). Error bars represent the standard deviation over 4000 lifelines considering a normal distribution. Following the models in [9], k_La was derived as the 900 s time-and-volume-averaged k_La of CO, with the error bars representing the standard deviation during that period, while the ₑirculation time t_c was estimated via t_m (1/4 of the 95% mixing time of 90 s in every case [52]).

on their time-averaged biomass-specific uptake, product formation rates, and observed concentrations, were compared with the results from the model with constant dissolved gas concentrations (Fig. 5). To check the correspondence of the model predictions with experimental trends and values, we retrieved q_i and calculated $c_{L,CO}$ for several chemostat experiments. Overall, the trends and the values of the experimental studies corresponded well to those predicted by the model.

The models overestimate the average CO uptake rate compared to experimental data at high $c_{L,CO}$ (Fig. 5a). This led to a rather constant q_{CO} while there was a large spread in $c_{L,CO}$ in our model, rendering q_{CO} unsuitable for trend analysis. This is partly due to the calibration of the CRD model, which predicted q_{CO} consistently around 1 $mol_{CO}mol_x^{-1}h^{-1}$ while more variation was observed in the experimental data [38]. The (Haldane) kinetic models that have been developed so far (e.g., [38,60,61]), are unable to predict the high q_{CO} that is observed experimentally (e.g., [35]). We noticed wide variability in q_{CO} in chemostat experiments with low $c_{L,CO}$. Due to this variability and the lack of models that adequately link $c_{L,CO}$ and q_{CO}, we are unable, at this point, to establish any hypotheses or trends based on q_{CO}, and decided to focus our analysis on the role of $c_{L,CO}$ on the product spectrum.

Acetate production (Fig. 5b) is slightly underestimated by the model in all scenarios, but the trend clearly corresponds: more acetate is produced at higher $c_{L,CO}$. The trend of q_{EtOH} and the ethanol-per-electron yield (Fig. 5c,d) match surprisingly well with the experimental data, and is clearly inverse to the acetate trend: more ethanol is produced at lower $c_{L,CO}$. This relationship is also visible in the acetate-per-ethanol

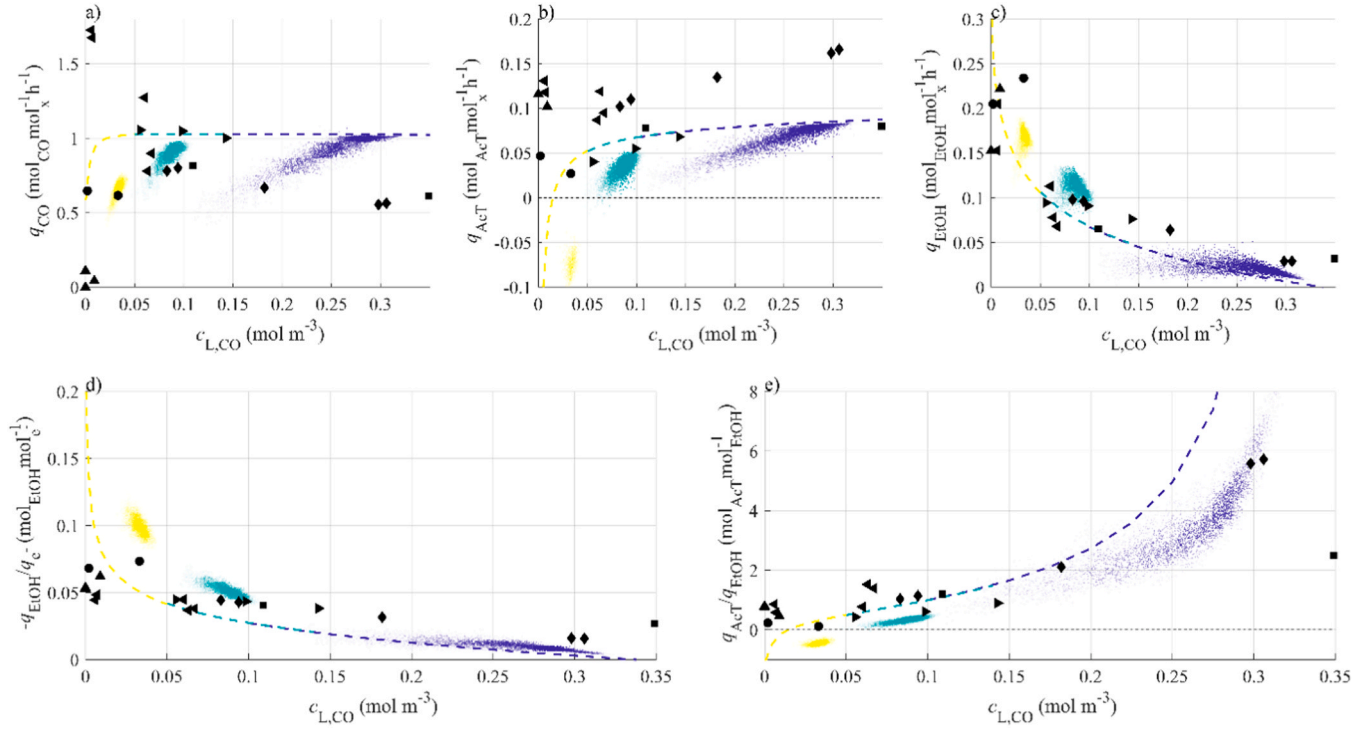

Fig. 5. Comparison of lifeline-averages from the CFD-CRD model with the constant concentration model and experimental data. The average biomass-specific rates and yields are plotted against the average dissolved $c_{L,CO}$: a) q_{CO}, b) q_{AcT}, c) q_{EtOH}, d) the electron-to-ethanol yield q_{EtOH}/q_{e^-} ($q_{e^-} = ½(q_{CO} + q_{H2})$, and e) the acetate-per-ethanol ratio q_{Ac}/q_{EtOH}. The scatters, with varying transparency to reduce overplotting, represent 900 s averages for ~4000 lifelines for each c_x simulation (blue 2.5; green 3.75; yellow 5 g L^{-1}), the dashed line simulations with constant dissolved gas concentrations at the indicated biomass concentrations, and the markers reconciled experimental chemostat data [38,56]: ◆ [57]; ■ [36] ($CO + H_2$); ● [36] (CO); ▲[58]; ◄ [35]. $c_{L,CO}$ in ►[59], was estimated using their provided k_La.

ratio (Fig. 5e), where it is clear that $q_{EtOH} > q_{AcT}$ at $c_{L,CO} < 0.1$ mol m^{-3}. Our model and experimental data suggest that ethanol is produced at the expense of acetate at lower $c_{L,CO}$, while acetate is produced at the expense of ethanol at high $c_{L,CO}$.

The CFD-CRD model suggests that the gradients expected at scale benefit ethanol production, since consistently a significant (~25%) higher q_{EtOH} and q_{EtOH}/q_{e^-} and lower acetate production are predicted, compared to the results obtained without concentration fluctuations ($p < 10^{-4}$ in all c_x cases using a one-sample *t*-test, wherein the distribution of lifelines is compared to the mean result of the constant concentration model in that respective range). Section 3.5 further explores potential reasons behind this behaviour. Another interesting observation is that at large-scale, population heterogeneity is likely to be observed, visible from the wide scattering of the lifeline-averages in Fig. 5. The relatively short simulation duration of the CFD-CRD model could be a factor underlying the scattering, but given the currently available computational resources longer two-way coupled simulations with such a resolution are practically unfeasible. For example, to match the long simulation time of the *P. chrysogenum* industrial fermentation (70 hours) with the current model setup, ~14 years of simulations would be required. The development of reduced order models (e.g., compartment models) could be a solution to alleviate this problem [24–26].

Our model, in conjunction with experimental data, indicates that $c_{L,CO}$ is a key factor influencing the onset of solventogenesis. At high $c_{L,CO}$, acetogenesis prevails; however, as $c_{L,CO}$ decreases below ~0.1 mol m^{-3}, ethanol production rate surpasses that of acetate production (e.g., solventogenesis). A phase guided by electron supply shortages and energy starvation has been observed at very low dissolved gas concentrations ($c_{L,CO} < 0.05$ mol m^{-3}). In this phase, there is a net consumption of acetate. Acetate is reduced to ethanol, with CO serving as an electron source essential for growth and maintenance (through ATP production via Rnf). As the re-oxidation of the electron carriers occurs via the AOR route, acetate – which freely diffused into the cell as acetic acid – is being converted into ethanol [34,46]. This phenomenon was also observed in the second reactor in [62], with biomass recycle and high CO conversion and probably very low $c_{L,CO}$, where both acetate and CO consumption resulted into very high ethanol productivity, although this particular result could also be linked to shortages of essential nutrients as vitamins and metals. It is well known that acetate supplementation enhances the ethanol productivity [55,63,64], while it has been demonstrated that exogenously introduced ^{13}C-labeled acetate was converted into ^{13}C-labeled ethanol on CO-grown *C. autoethanogenum* [64]. All these observations lend support to the feasibility of this starvation-induced metabolism at low $c_{L,CO}$.

A simple thermodynamic analysis could explain why more ethanol is produced at lower $c_{L,CO}$ (Table E.1). During ethanol production, more ATP is produced (~2 vs. 1.5 $mol_{ATP}/mol_{product}$) [34,65] since its production releases more energy (kJ/mol_{CO}) [66] compared to acetate production (1.5 $mol_{ATP}/mol_{product}$), and it is thus not a surprise that ethanol production relates to growth, confirmed both experimentally [35] and in our model (Figure E.3). When more CO is available, acetate might be produced since there is enough carbon and energy resource for growth, relating to the hypothesis of maximum energy dissipation [67]. The resulting acetic acid decreases pH (increasing the proton motive force used for energy generation), safeguarding sustainable growth in the future. From an evolutionary perspective, it might be that this presents a competitive advantage against other microorganisms [68], and thus a survival strategy in nature. Ethanol production via solventogenesis might then only be a (stress) reaction to preserve more energy at low dissolved gas concentrations, while in case with even lower $c_{L,CO}$, the starvation metabolism is employed for increased energy generation.

As large parts of the data used for the generation of Fig. 5 were outside the calibrated range of the model (i.e., $c_{L,CO} < 0.025$ mol m^{-3}), a similar figure was generated without considering data in this range (Figure E.1). Obviously, this led to higher average $c_{L,CO}$ and a lower spread in $c_{L,CO}$ amongst lifelines. More interestingly is the decreased q_{EtOH} for the 5 g L^{-1} case (that was also noted in Section 3.1), while the trends for all compounds remained similar among the complete $c_{L,CO}$ domain. The gradient still led to significant ($p < 10^{-4}$) increases in q_{EtOH}. The uncertainty in the very low $c_{L,CO}$ range requires caution for quantitative analysis under these conditions.

3.5. Metabolism of *C. autoethanogenum* during dynamic conditions

The effect of the dissolved gas concentration fluctuations in the EL-GLR on the concentrations of metabolites and the modelled rates are schematically depicted in Fig. 6. This representation allows us to follow the route of the carbon (blue lines) and electrons (green lines) and gives an impression on which processes drive the production of ethanol.

Following the carbon, a direct coupling between CO uptake and acetate synthesis is seen. The Wood-Ljungdahl pathway, represented with the ACAS flux (J_{ACAS}) in Fig. 6, is almost always activate with fairly constant rate, although it gets an impulse during a period at low $c_{L,CO}$ due to the increased NADH availability in the cell. Consequently, the AcCoA concentration pattern follows the peaks of dissolved CO, although it is slightly influenced by the periods at low CO. The net amount of AcCoA slowly decreased during the analysis, a trend also observed in the simulation with constant dissolved gas concentrations (Figure A.2). The rate of acetate formation (J_{AcS}) follows the CO availability, albeit slightly lower than J_{ACAS}, since small amounts of AcCoA are also being used for the formation of biomass and 2,3-BDO. The cell is continuously busy with the acetate import/export cycle: High rates of J_{AcX} and J_{HAcD} were predicted (~0.45 and ~0.40 mol $mol_x^{-1}h^{-1}$, respectively), around three times higher than its formation rate via J_{AcS}. Despite these efforts, there is still some acetate accumulation in the cell. In the case with less biomass, there is more acetate export, but also more intracellular acetate accumulation, while lower intracellular acetate concentrations are obtained in the case with more biomass. In the latter case, there is net consumption of acetic acid ($J_{HAcD} > J_{AcX}$), which leads to increased ethanol production rates; the starvation-induced metabolism, as explained in the previous section.

Most (~75%) of the consumed CO is being used for electron capture with CODH, thereby producing CO_2 ($J_{CODH} > J_{FDH}$), and reducing ferredoxin. $c_{Fd^{2-}_{red}}$ follows the same profile as $c_{L,CO}$, but its fluctuations are slower and less steep, showing its electron buffering capacity. Around 70% of the reduced ferredoxin is re-oxidized due to Rnf activity, the enzyme that shuttles the electrons from Fd^{2-}_{red} to NAD^+ [69], and translocates protons across the cell membrane for the generation of the proton motive force and ATP [32]. NADH, in turn, is mostly used to drive the Wood-Ljungdahl pathway (ACAS) and for the production of the NADPH (via Nfn) that is required for ACAS and FDH.

In a period with low $c_{Fd^{2-}_{red}}$, q_{H2} is increased which relates to increased q_{EtOH} (Figure C.2, E.3). The first observation could relate to inhibition of q_{H2} by reduced ferredoxin, while a similar (but weaker) trend was obtained for CO uptake. This caused that decreased CO and H_2 uptake rates were actually observed at high reduced ferredoxin concentrations, and not at high CO or H_2 concentrations *per se* (cf., Figure C.1 and C.2). Inhibition of gas uptake could thus, next to binding of CO to hydrogenases, also be explained by a highly reduced intracellular state (i.e., too high intracellular concentrations of electron carriers), as was hypothesized before [70]. Our model results and chemostat experiments [35,36] show that q_{H2} proportionally relates to q_{EtOH}. The ferredoxin that is reduced due to hydrogen uptake is probably instantaneously being re-oxidized again to drive EtS and Rnf (Fig. 6), because of the temporary lack of reducing equivalents, this mechanism guarantees electron inflow even at $c_{L,CO}$.

At dynamic conditions, a direct relationship between and $c_{Fd^{2-}_{red}}$ and $c_{L,CO}$ ($c_{Fd^{2-}_{red}}$ increases with $c_{L,CO}$) is observed (Fig. 7a), while $c_{Fd^{2-}_{red}}$ shows an inverse hyperbolic relationship to q_{EtOH} (Fig. 7b). This indicates that, irrespective of other phenomena occurring in the cell, q_{EtOH} is mostly determined by the temporal $c_{Fd^{2-}_{red}}$. If other phenomena would have

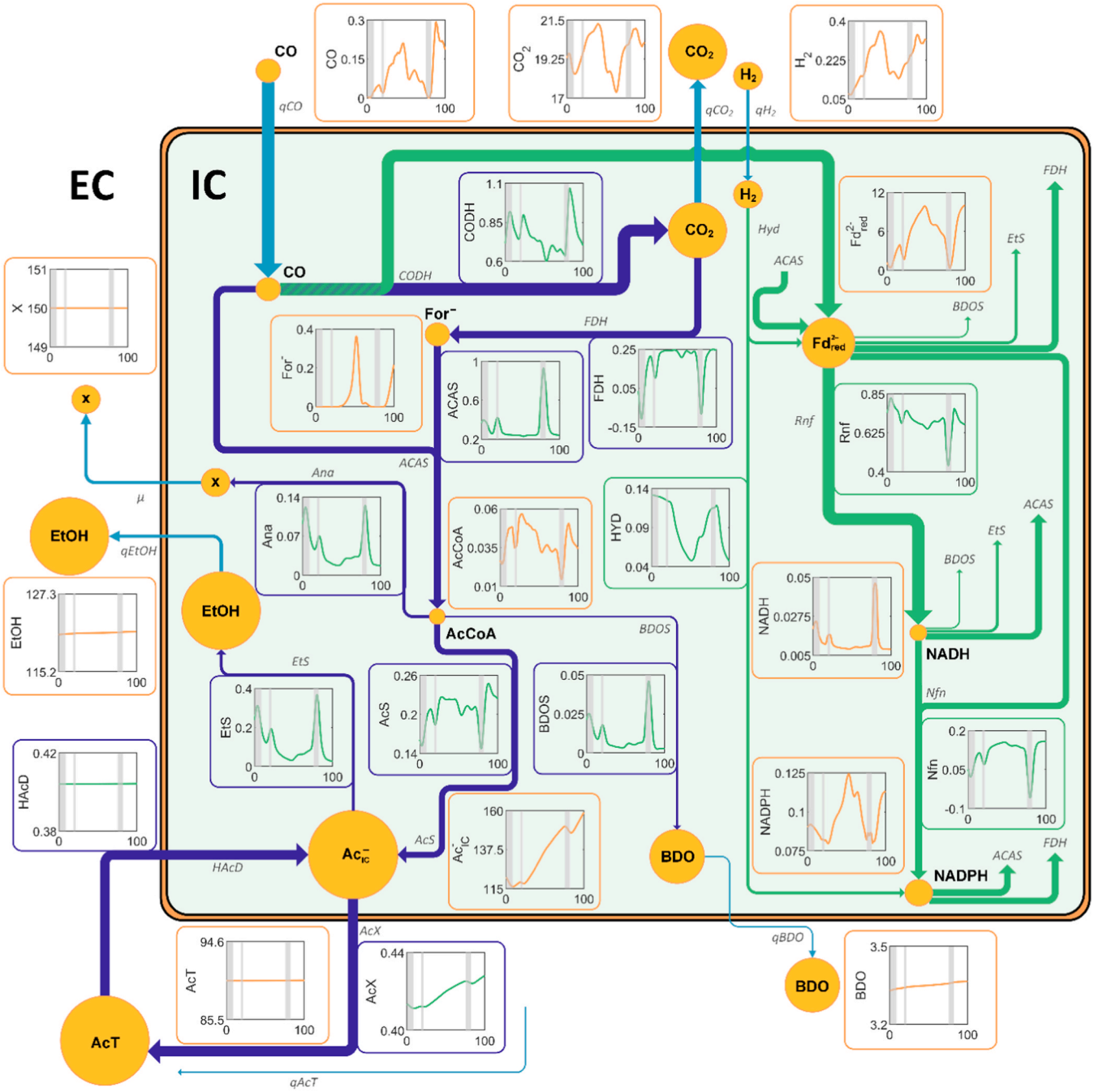

Fig. 6. Metabolism of *C. autoethanogenum* during large-scale syngas fermentation. 100 seconds of a lifeline for the case with 3.75 $g_x\ L^{-1}$ is shown with its concentration (in mol m^{-3}) and rate (in mol $mol_x^{-1}h^{-1}$) fluctuations. Pool sizes and arrow thickness are approximative to the median concentrations and rates during the whole lifeline. The metabolism in the cases with 2.5 and 5 $g_x\ L^{-1}$ are provided in the supplementary material (Figure F.1 and F.2). Shaded areas in the plots mark zones with $c_{L,CO} < 0.025$ mol m^{-3}.

influenced q_{EtOH}, a larger spread in q_{EtOH} would be observed at the each $c_{Fd^{2-}_{red}}$. The NADH concentration shows a strong relationship with $c_{Fd^{2-}_{red}}$ (c_{NADH} decreases with $c_{Fd^{2-}_{red}}$), so on its turn c_{NADH} proportionally relates to q_{EtOH}, as was shown experimentally [34,39,71]. We could thus predict that, at some point, with low $c_{L,CO}$ and thus low $c_{Fd^{2-}_{red}}$, high amounts of NADH and consequentially increased q_{EtOH} are obtained. The increased q_{EtOH} is due to decreases acetate production (Fig. 7b), this way conserving mass balances (Figure A.5).

The delay that is observed between CO uptake and ethanol production (a peak in q_{EtOH} ~50 s; Fig. 6) is present when $c_{L,CO}$ and, and consequentially $c_{Fd^{2-}_{red}}$, decreased enough to stimulate ethanol production. For example, no clear increase in q_{EtOH} is observed after peaks in $c_{L,CO}$, until $c_{Fd^{2-}_{red}}$ decreases to ~6 mol m^{-3}, when also J_{AcS} slows down, reducing acetate production. Therefore, the delay is caused by the dynamics in the EL-GLR and causes that the microorganisms cycle between two states: one state with high $c_{L,CO}$ and $c_{Fd^{2-}_{red}}$, and thus low c_{NADH} and q_{EtOH}, and another state with low $c_{L,CO}$ and $c_{Fd^{2-}_{red}}$, but with increased c_{NADH} and q_{EtOH}.

Dissolved CO concentration fluctuations (e.g., increased c_x (Figure F.2)) induce the mentioned redox cycling and ethanol production. This happens at the expense of the intracellular acetate pool and J_{AcS}, and in the long term at the expense of the extracellular acetate

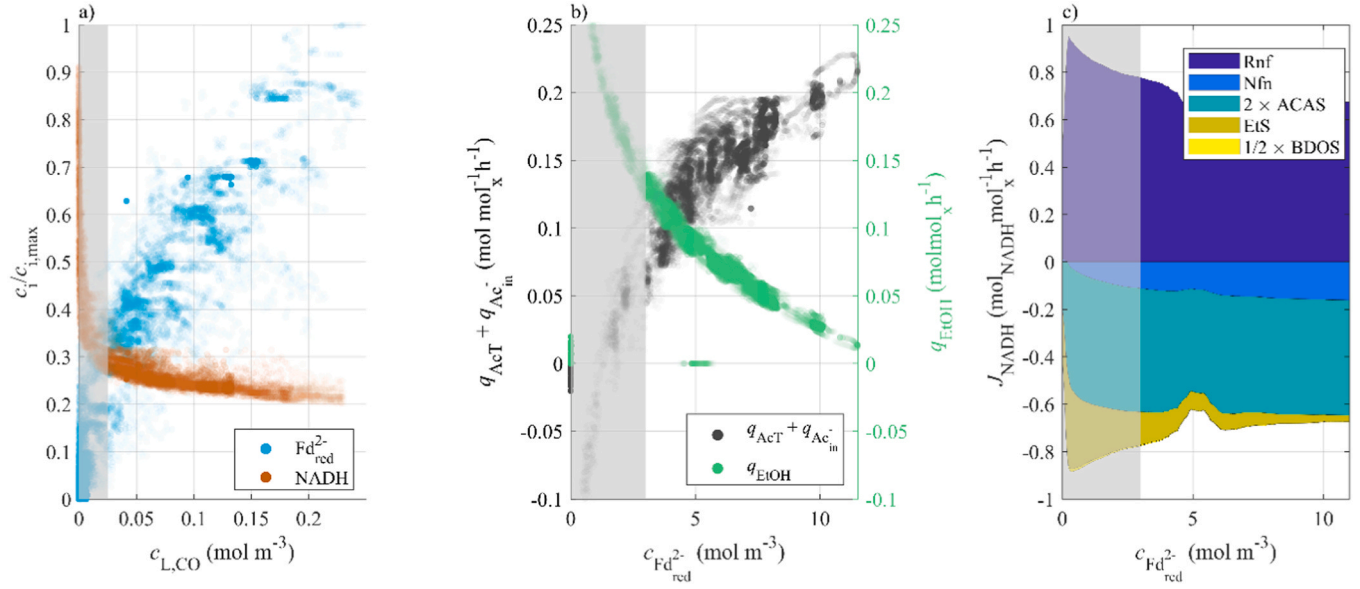

Fig. 7. Mechanism towards ethanol production in a lifeline. a) The relationship between the concentration of electron carriers Fd^{2-}_{red} (blue) and NADH (orange) is shown and their corresponding $c_{L,CO}$ ($c_{Fd^{2-}_{red},max}$ = 11.5 mol m^{-3}, $c_{NADH,max}$ = 0.04 mol m^{-3}). b) the relationships between acetate production (extracellular + intracellular) (black) and ethanol production (green) with $c_{Fd^{2-}_{red}}$. c) the rates of NADH production (Rnf, darkblue) and consumption (Nfn, light blue; ACAS, green; Ethanol Synthesis, gold; BDO Synthesis; yellow) as function of $c_{Fd^{2-}_{red}}$. The scatters mark temporal observations during a lifeline (between 100 and 1000 s), and their density denotes the probability of occurrence. Figure c) is an energy balance that can be made since $\tau_{NADH} << \tau_{Fd^{2-}_{red}}$. Shaded areas mark zones with $c_{L,CO}$ < 0.025 mol m^{-3}.

concentration. The non-linear behaviour of metabolism (here described by lin-log kinetics), the irregular duration and the large variation in $c_{L,CO}$ in low concentration zones (< 0.05 mol m^{-3}) might cause that non-linear increases in ethanol productivity are observed upon concentration fluctuations. The effect of such variations has never been determined experimentally, a good start for experimental verification would be the developed scale-down simulator in our previous paper [9].

The only reaction that reduces NAD^+ to NADH in our model is the Rnf, which is active in the whole domain of reduced ferredoxin concentrations (Fig. 7c). The resulting NADH is mostly used in the Wood-Ljungdahl pathway (by ACAS), while a small fraction is used for NADPH generation, which is also required in ACAS. At lower $c_{L,CO}$ and $c_{Fd^{2-}_{red}}$, Rnf activity increases while the majority of the resulting NADH is re-oxidized via the Ethanol Synthesis pathway. Thus, the increased Rnf activity at slower $c_{Fd^{2-}_{red}}$, can be associated to increases in q_{EtOH}. Metabolic models have previously predicted that increased Rnf activity relates with increased ethanol production in syngas fermenting *Clostridium* spp. [35,51,57,58], although such relationships have never been observed experimentally. A proportional relationship between Rnf and ethanol production was found, however, in *C. thermocellum* grown on cellobiose [72].

The CFD-CRD model also predicts a coupling between ethanol production and growth rate. At higher growth rates, more ethanol is produced (Figure E.3) which complies with experimental observations (e.g., [35]). This might be because growth happens when there is more ATP available and that is the case when Rnf is more active as Rnf increases the proton motive force. No relation, however, between acetate production (q_{AcT}) and growth rate was observed (Figure E.3), which might explain the contrasting experimental data regarding growth rate.

3.6. Emerging hypotheses

By mathematically modelling syngas fermentation, we derived a mechanistic understanding on how the dissolved gas concentration (and its fluctuations) influence the product spectrum of *C. autoethanogenum*, which we could support with experimental evidence. Thus far, experimentalists made statements that, for example, *i)* higher dilution rates increase q_{EtOH} [35,46], *ii)* that lower mass transfer rates result in lower CO concentrations [55], or *iii)* that increased pressure leads to increased formate production [53]. But, by linking $c_{L,CO}$ (and potentially q_{CO}) to the product spectrum, we could merge such statements into one overarching explanation, by suggesting that *i)* q_{EtOH} is increased at lower $c_{L,CO}$, *ii)* that acetogenesis occurs at increased $c_{L,CO}$ and that *iii)* formate accumulates in over-reduced situations (very high $c_{L,CO}$ and $c_{Fd^{2-}_{red}}$). In practice, this might mean that, for example, the faster growth in [35], coupled to high q_{CO}, might have let to the fall in $c_{L,CO}$ so that q_{EtOH} is increased. The inverse relationship between q_{CO} and $c_{L,CO}$ indicates a very low K_S (supported by thermodynamics [66]) and low inhibition constant K_I for Haldane kinetics, consistent with the experimentally expected fast CO uptake [31,35,73]. Meanwhile, the increased acetate concentration should be noted in the discussion [55,63]. To test our observations, the influence of $c_{L,CO}$ on q_{CO} and q_{EtOH} should be studied in chemostats with CO measurements (e.g., using the protocol in [74] or estimated following [56]) and with fixed operating conditions (i.e., constant growth rates and liquid phase concentrations). As a result, researchers on gas fermentation should link their results to microbial experiences, and thus dissolved gas concentration, and not to operational factors at the reactor-level such as pressure, dilution, or mass transfer rate (e.g., governed by stirrer speed).

The trends in Fig. 7b might seem remarkable, from a steady-state point of view. For example, in chemostats it has been observed that increased electron (or dissolved gas) uptake rates increases q_{EtOH} [35,46]. As electron uptake is associated to reduction of ferredoxin, which should lead to increased c_{NADH} and thus q_{EtOH}, it might seem controversial that, in our results, high q_{EtOH} is only obtained at low $c_{Fd^{2-}_{red}}$. We identified four hypotheses why we observed this trend in Fig. 7b. The first *i)* is that $c_{Fd^{2-}_{red}}$ is around 100 times higher than c_{NADH}, causing that each NAD^+ molecule needs to be reduced and re-oxidized 100 times in order to re-oxidize 100 ferredoxin molecules. This might cause that NAD^+ is the limiting component in the Rnf reaction. This hypothesis might be tested by determining the $c_{Fd^{2-}_{red}}/c_{NADH}$ ratio during over-reduced and under-reduced conditions, although it is experimentally very challenging and never done so far in gas fermenting bacteria. Another hypothesis *ii)* might be related to the thermodynamics of the

AOR pathway (acetate to ethanol reduction) as discussed in [39], wherein it is stated that – at constant reduced ferredoxin concentrations, due to long-lasting batch conditions – there is a linear relationship between the NADH/NAD^+ ratio and the ethanol-to-acetate ratio (similar to our results, since q_{AcT} decreases when q_{EtOH} increases). If the Fd^{2-}_{red}/Fd_{ox} ratio is increased in their model, at a constant ethanol-to-acetate ratio, a lower NADH/NAD^+ ratio may be expected, similar to our model results in Fig. 7. Furthermore *iii)*, the timescale in a chemostat (order of days) is significantly longer than that of liquid circulation and mass transfer (usually > 20 s) and intracellular metabolite and uptake (< 1 s; Fig. 3), which could lead to concentration gradients at lab-scale and similar $c_{Fd^{2-}_{red}}/c_{NADH}$ fluctuations. The last hypothesis *iv)* relates to binding of dissolved CO to iron-sulfur complexes present in Rnf [69,75] or in ferredoxins [30], similarly to its binding to the Fe-S complexes in hydrogenases [4,76,77], and thereby inhibiting Rnf activity. When $c_{L,CO}$ (and thus $c_{Fd^{2-}_{red}}$) decreases, less Rnf inhibition might be obtained causing that its rate could be increased.

Clearly, too little is known at this moment on the metabolism of acetogens at low dissolved gas concentrations, and during dynamic conditions. To improve our understanding, experiments should be performed wherein *C. autoethanogenum* is exposed to short (5 – 30 s) shortages in $c_{L,CO}$, so that the effect of a metabolic stall can be studied, which can be used for model updates. Development of measurement methods for $c_{Fd^{2-}_{red}}$ and dissolved CO at such conditions would be highly relevant. The ratio of reduced-to-oxidized ferredoxin was estimated to be high during batch fermentations, while the NADH/NAD^+ ratio was more dynamic [39], although such results have not yet been obtained from chemostats or during conditions with dynamic gas supply, such as in the scale-down simulator described in [9].

We realize that the lin-log structure of the CRD-model bears several limitations. Results of lin-log models are good estimations around the reference conditions (i.e., around which they have been calibrated) [43], but in the CFD-CRD model, intra- and extracellular conditions far away from the reference concentration may locally occur (see Table A.1). For example, the small "gap" in Fig. 7c, corresponds to the reference concentration of NADH (i.e., 0.011 mol m^{-3}, Fig. 7b), deviations in this reference concentration might impact our model results and interpretation. Despite the implemented rate limitation modifications that were required for model stability, the CFD-CRD model still contained, although significantly dampened, numerical errors (Fig. 2). We would therefore **not** recommend to use the lin-log structure for CRD models if they are to be coupled with CFD models, but instead stick to hyperbolic equations, analogous to [78,79] using mechanistic rate equations for intracellular reactions. Another limitation is the ultra-long simulation time of our CFD-CRD model, due to the large number of particles simulated (N_p = 80,000), the short Δt_{IC} (0.1 ms) for integration, and poor parallelization of the particle-based metabolic model. As a consequence, our simulations had a significant power consumption and environmental burden (~0.45 MWh and ~200 kg CO_2). The development and parametrization time of the kinetic model took one year, and incorporation in the CFD model lasted around 6 months, so that development of CFD-CRD models should not be considered to be trivial. This demonstrates the balancing act between model purpose, complexity and resource availability.

Lastly, the CRD model could be improved by implementing several additional reactions. An export and back-diffusion cycle for formate should be added, together with the reaction for CO_2 reduction to formate with H_2. Furthermore, there is some evidence that hydrogen can be produced from formate, using a $NADP^+$-based hydrogenase [70], which might be the cause of the simultaneous formate and hydrogen production in [55]. The parameters regarding the acetate export cycle are probably not well calibrated in the CRD model, since the model at low c_x predict large intracellular accumulation of acetate (Figure A.2). Implementation of an ATP balance or maintenance might also improve the model in this respect. The clear spatial discrepancy between ethanol and acetate production zones might result in significant pH variations, in turn affecting the local q_{AcT}/q_{EtOH} ratio. Metabolic models that can predict variations in extracellular pH should be developed, and coupled with CFD to minimise the effect of non-ideal mixing and improve pH buffering.

3.7. Towards better gas fermentation bioreactors

The presented CFD-CRD model and its results could enable ways towards rational optimization of gas fermentation, by adjusting operating conditions, the reactor geometry, and by strain engineering.

In terms of reactor operation, mass transfer limitations are desired: In case there are no mass transfer limitations, CO inhibition prevails, leading to low CO and H_2 conversion rates, while lower $c_{L,CO}$ and higher conversion rates are obtained when there are mass transfer limitations [9]. In order to sustainably obtain high q_{EtOH} at industrial-scale, the average $c_{L,CO}$ as experienced by the micro-organisms should be kept in a narrow range, around the predicted optimum $c_{L,CO}$ of ~0.05 mol m^{-3} according to our model (Fig. 5e). A lower $c_{L,CO}$ will induce too much acetate consumption, while at higher $c_{L,CO}$ acetate will be produced at the expense of ethanol. When operating in a mass transfer-limited regime, high operational flexibility regarding $c_{L,CO}$ can be obtained via the incoming gas flow rate, as this directly influences the gas hold-up and thus the mass transfer rate. For example, when there is too much acetate production ($c_{L,CO}$ is too high), one could decrease the gas flow rate, which would decrease $c_{L,CO}$, so that produced acetate might be consumed again, leading to high ethanol productivities.

In terms of reactor geometry, clear zonation was obtained in the EL-GLR (Fig. 3), with CO uptake and ferredoxin reduction in one zone, and the ferredoxin re-oxidation and ethanol production in the other zone. As both processes can happen quite fast (order of seconds), and cellular transition between the zones was found advantageous for ethanol production, forced zonation can be an interesting way to increase ethanol productivity. To improve industrial-scale reactor design, future (lab and modelling) research could focus on determination of the ideal residence times in both zones, which can be implemented by altering the interior and exterior reactor geometry, and related operation conditions.

Lastly, increases in J_{Rnf} were found to be directly related to increases in q_{EtOH} (Fig. 7c). Overexpression of Rnf (with deletion of hydrogenase) has been proven as a viable method to increase ethanol production in *C. thermocellum* [72]. Overexpressing Rnf may be a method to amplify J_{Rnf} at high $c_{Fd^{2-}_{red}}$ and might increase q_{EtOH} even further in *C. autoethanogenum*.

4. Conclusion

In this work, we coupled a CFD model of an industrial-scale reactor for gas fermentation to a metabolic kinetic model to study the influence of the dissolved CO concentration and its gradient on the productivity and product spectrum of *C. autoethanogenum*. By comparing our model results with experimental data, we uncovered that the dissolved CO concentration (and potentially q_{CO}) is a major factor steering the product spectrum: Very low $c_{L,CO}$ (< 0.05 mol m^{-3}) result in high ethanol production rates by reducing extracellular acetic acid, in a starvation-induced metabolism, slightly higher concentrations (0.05 < $c_{L,CO}$ < 0.1 mol m^{-3}) were related to solventogenesis (CO to ethanol conversion), while high concentrations ($c_{L,CO}$ > 0.1 mol m^{-3}) were associated with acetate production. The gradient at industrial-scale led to a ~25% increase in ethanol production rate and yield, at the expense of acetate production. This increase was explained by redox cycles of ferredoxin and NAD^+, which are imposed when there is a gradient in $c_{L,CO}$. Due to the gradient, the concentration of reduced ferredoxin gradually decreases, while NADH increases due to Rnf activity. The re-oxidation of the resulting NADH caused increased ethanol production rates. We identified several hypotheses to support these results, made suggestions

for follow-up research and developed a mechanistic understanding on the gas fermentation process.

CRediT authorship contribution statement

Lars Puiman: Writing – review & editing, Writing – original draft, Software, Methodology, Investigation, Formal analysis, Conceptualization. **Eduardo Almeida Benalcázar:** Writing – review & editing, Software, Formal analysis, Conceptualization. **Cristian Picioreanu:** Writing – review & editing, Supervision, Conceptualization. **Henk Noorman:** Writing – review & editing, Supervision, Conceptualization. **Cees Haringa:** Writing – review & editing, Supervision, Software, Conceptualization.

Declaration of Generative AI and AI-assisted technologies in the writing process

During the preparation of this work the author(s) used ChatGPT 3.5 in order to improve language and readability. After using this tool/service, the author(s) reviewed and edited the content as needed and take(s) full responsibility for the content of the publication.

Declaration of Competing Interest

The authors declare that they have no known competing financial interests or personal relationships that could have appeared to influence the work reported in this paper.

Data Availability

The UDF used in the CFD-CRD model, the FLUENT case file, the developed scripts in C on the metabolic model and the MATLAB scripts for post-processing are available at https://doi.org/10.4121/bb567f3e-a146-4ad8-8074-3b3fee387a0a.

Acknowledgement

This work is written as part of the MicroSynC research programme (project number P16–10/5) and is (partly) financed by the Netherlands Organization for Scientific Research (NWO). This work used the Dutch national e-infrastructure with the support of the SURF Cooperative using grant no. EINF-4918. We would like to thank our colleagues in the TU Delft Bioprocess Engineering section for their input into valuable discussions, with special mentioning to Adrie Straathof, Rob van der Lans, Marina Elisiário, Rik Volger, and Héctor Maldonado de Léon.

Appendix A. Supporting information

Supplementary data associated with this article can be found in the online version at doi:10.1016/j.bej.2024.109330.

References

[1] N. Fackler, B.D. Heijstra, B.J. Rasor, H. Brown, J. Martin, Z. Ni, K.M. Shebek, R. R. Rosin, S.D. Simpson, K.E. Tyo, R.J. Giannone, R.L. Hettich, T.J. Tschaplinski, C. Leang, S.D. Brown, M.C. Jewett, M. Köpke, Stepping on the gas to a circular economy: accelerating development of carbon-negative chemical production from gas fermentation, Annu. Rev. Chem. Biomol. Eng. 12 (2021) 439–470, https://doi.org/10.1146/ANNUREV-CHEMBIOENG-120120-021122.

[2] M. Köpke, S.D. Simpson, Pollution to products: recycling of 'above ground' carbon by gas fermentation, Curr. Opin. Biotechnol. 65 (2020) 180–189, https://doi.org/10.1016/j.copbio.2020.02.017.

[3] F.E. Liew, R. Nogle, T. Abdalla, B.J. Rasor, C. Canter, R.O. Jensen, L. Wang, J. Strutz, P. Chirania, S. De Tissera, A.P. Mueller, Z. Ruan, A. Gao, L. Tran, N. L. Engle, J.C. Bromley, J. Daniell, R. Conrado, T.J. Tschaplinski, R.J. Giannone, R. L. Hettich, A.S. Karim, S.D. Simpson, S.D. Brown, C. Leang, M.C. Jewett, M. Köpke, Carbon-negative production of acetone and isopropanol by gas fermentation at industrial pilot scale, 2022 403, Nat. Biotechnol. 40 (2022) 335–344, https://doi.org/10.1038/s41587-021-01195-w.

[4] F.M. Liew, M.E. Martin, R.C. Tappel, B.D. Heijstra, C. Mihalcea, M. Köpke, Gas Fermentation-A flexible platform for commercial scale production of low-carbon-fuels and chemicals from waste and renewable feedstocks, Front. Microbiol. 7 (2016) 1–28, https://doi.org/10.3389/fmicb.2016.00694.

[5] L. Puiman, B. Abrahamson, R.G.J.M. van der Lans, C. Haringa, H.J. Noorman, C. Picioreanu, Alleviating mass transfer limitations in industrial external-loop syngas-to-ethanol fermentation, Chem. Eng. Sci. 259 (2022) 117770, https://doi.org/10.1016/J.CES.2022.117770.

[6] L. Puiman, M.P. Elisiário, L.M.L. Crasborn, L.E.C.H. Wagenaar, A.J.J. Straathof, C. Haringa, Gas mass transfer in syngas fermentation broths is enhanced by ethanol, Biochem. Eng. J. 185 (2022) 108505, https://doi.org/10.1016/J.BEJ.2022.108505.

[7] A.R. Lara, E. Galindo, O.T. Ramírez, L.A. Palomares, Living with heterogeneities in bioreactors, 2006, Mol. Biotechnol. 343 (34) (2006) 355–381, https://doi.org/10.1385/MB:34:3:355.

[8] G. Nadal-Rey, D.D. McClure, J.M. Kavanagh, S. Cornelissen, D.F. Fletcher, K. V. Gernaey, Understanding gradients in industrial bioreactors, Biotechnol. Adv. 46 (2021) 107660, https://doi.org/10.1016/J.BIOTECHADV.2020.107660.

[9] L. Puiman, E. Almeida Benalcázar, C. Picioreanu, H.J. Noorman, C. Haringa, Downscaling Industrial-Scale Syngas Fermentation to Simulate Frequent and Irregular Dissolved Gas Concentration Shocks, Bioengineering 10 (2023) 1–22, https://doi.org/10.3390/bioengineering10050518.

[10] M. Kuschel, F. Siebler, R. Takors, Lagrangian Trajectories to Predict the Formation of Population Heterogeneity in Large-Scale Bioreactors, Bioengineering 4 (2017) 27, https://doi.org/10.3390/bioengineering4020027.

[11] M. Pigou, J. Morchain, Investigating the interactions between physical and biological heterogeneities in bioreactors using compartment, population balance and metabolic models, Chem. Eng. Sci. 126 (2015) 267–282, https://doi.org/10.1016/j.ces.2014.11.035.

[12] A. Lapin, J. Schmid, M. Reuss, Modeling the dynamics of E. coli populations in the three-dimensional turbulent field of a stirred-tank bioreactor-A structured-segregated approach, Chem. Eng. Sci. 61 (2006) 4783–4797, https://doi.org/10.1016/j.ces.2006.03.003.

[13] W. Olughu, G. Deepika, C. Hewitt, C. Rielly, Insight into the large-scale upstream fermentation environment using scaled-down models, J. Chem. Technol. Biotechnol. 94 (2019) 647–657, https://doi.org/10.1002/jctb.5804.

[14] M. Löffler, J.D. Simen, G. Jäger, K. Schäferhoff, A. Freund, R. Takors, Engineering E. coli for large-scale production – Strategies considering ATP expenses and transcriptional responses, Metab. Eng. 38 (2016) 73–85, https://doi.org/10.1016/j.ymben.2016.06.008.

[15] E.A. Sandoval-Basurto, G. Gosset, F. Bolivar, O.T. Ramírez, Culture of Escherichia coli under dissolved oxygen gradients simulated in a two-compartment scale-down system: Metabolic response and production of recombinant protein, Biotechnol. Bioeng. 89 (2005) 453–463, https://doi.org/10.1002/bit.20383.

[16] F. Siebler, A. Lapin, M. Hermann, R. Takors, The impact of CO gradients on C. ljungdahlii in a 125 m3 bubble column: Mass transfer, circulation time and lifeline analysis, Chem. Eng. Sci. 207 (2019) 410–423, https://doi.org/10.1016/j.ces.2019.06.018.

[17] X. Li, D. Griffin, X. Li, M.A. Henson, Incorporating hydrodynamics into spatiotemporal metabolic models of bubble column gas fermentation, Biotechnol. Bioeng. 116 (2019) 28–40, https://doi.org/10.1002/bit.26848.

[18] A. Lapin, D. Müller, M. Reuss, Dynamic behavior of microbial populations in stirred bioreactors simulated with Euler-Lagrange methods: Traveling along the lifelines of single cells, Ind. Eng. Chem. Res. 43 (2004) 4647–4656, https://doi.org/10.1021/IE030786K/ASSET/IMAGES/LARGE/IE030786KF00007.JPEG.

[19] J. Morchain, J.-C. Gabelle, A. Cockx, Coupling of biokinetic and population balance models to account for biological heterogeneity in bioreactors, AIChE J. 59 (2013) 369–379, https://doi.org/10.1002/aic.13820.

[20] C. Haringa, W. Tang, G. Wang, A.T. Deshmukh, W.A. van Winden, J. Chu, W. M. van Gulik, J.J. Heijnen, R.F. Mudde, H.J. Noorman, Computational fluid dynamics simulation of an industrial P. chrysogenum fermentation with a coupled 9-pool metabolic model: Towards rational scale-down and design optimization, Chem. Eng. Sci. 175 (2018) 12–24, https://doi.org/10.1016/j.ces.2017.09.020.

[21] W. Tang, A.T. Deshmukh, C. Haringa, G. Wang, W. van Gulik, W. van Winden, M. Reuss, J.J. Heijnen, J. Xia, J. Chu, H.J. Noorman, A 9-pool metabolic structured kinetic model describing days to seconds dynamics of growth and product formation by *Penicillium chrysogenum*, Biotechnol. Bioeng. 114 (2017) 1733–1743, https://doi.org/10.1002/bit.26294.

[22] D.D. McClure, J.M. Kavanagh, D.F. Fletcher, G.W. Barton, Characterizing bubble column bioreactor performance using computational fluid dynamics, Chem. Eng. Sci. 144 (2016) 58–74, https://doi.org/10.1016/J.CES.2016.01.016.

[23] G. Nadal-Rey, J.M. Kavanagh, B. Cassells, S. Cornelissen, D.F. Fletcher, K. V. Gernaey, D.D. McClure, Modelling of industrial-scale bioreactors using the particle lifeline approach, Biochem. Eng. J. 198 (2023) 108989, https://doi.org/10.1016/j.bej.2023.108989.

[24] C. Haringa, W. Tang, H.J. Noorman, Stochastic parcel tracking in an Euler–Lagrange compartment model for fast simulation of fermentation processes, Biotechnol. Bioeng. 119 (2022) 1849–1860, https://doi.org/10.1002/bit.28094.

[25] G. Nadal-Rey, D.D. McClure, J.M. Kavanagh, B. Cassells, S. Cornelissen, D. F. Fletcher, K.V. Gernaey, Development of dynamic compartment models for industrial aerobic fed-batch fermentation processes, Chem. Eng. J. 420 (2021) 130402, https://doi.org/10.1016/J.CEJ.2021.130402.

[26] J. Le Nepvou De Carfort, T. Pinto, U. Krühne, An Automatic Method for Generation of CFD-Based 3D Compartment Models: Towards Real-Time Mixing Simulations, Bioengineering 11 (2024) 1–17, https://doi.org/10.3390/bioengineering11020169.

[27] G. Wang, C. Haringa, W. Tang, H. Noorman, J. Chu, Y. Zhuang, S. Zhang, Coupled metabolic-hydrodynamic modeling enabling rational scale-up of industrial bioprocesses, Biotechnol. Bioeng. 117 (2020) 844–867, https://doi.org/10.1002/BIT.27243.
[28] F.S.F. Hartmann, I.A. Udugama, G.M. Seibold, H. Sugiyama, K.V. Gernaey, Digital models in biotechnology: Towards multi-scale integration and implementation, Biotechnol. Adv. 60 (2022) 108015, https://doi.org/10.1016/j.biotechadv.2022.108015.
[29] A.J.J. Straathof, S.A. Wahl, K.R. Benjamin, R. Takors, N. Wierckx, H.J. Noorman, Grand Research challenges for sustainable industrial biotechnology, Trends Biotechnol. 37 (2019) 1042–1050, https://doi.org/10.1016/j.tibtech.2019.04.002.
[30] K. Schuchmann, V. Müller, Autotrophy at the thermodynamic limit of life: a model for energy conservation in acetogenic bacteria, Nat. Rev. Microbiol. 12 (2014) 809–821, https://doi.org/10.1038/nrmicro3365.
[31] S.W. Ragsdale, E. Pierce, Acetogenesis and the Wood-Ljungdahl pathway of CO2 fixation, Biochim. Biophys. Acta - Proteins Proteom. 1784 (2008) 1873–1898, https://doi.org/10.1016/j.bbapap.2008.08.012.
[32] J. Mock, Y. Zheng, A.P. Mueller, S. Ly, L. Tran, S. Segovia, S. Nagaraju, M. Köpke, P. Dürre, R.K. Thauer, Energy conservation associated with ethanol formation from H2 and CO2 in Clostridium autoethanogenum involving electron bifurcation, J. Bacteriol. 197 (2015) 2965–2980, https://doi.org/10.1128/JB.00399-15.
[33] Z.Y. Liu, D.C. Jia, K.Di Zhang, H.F. Zhu, Q. Zhang, W.H. Jiang, Y. Gu, F.L. Li, Ethanol metabolism dynamics in Clostridium ljungdahlii grown on carbon monoxide, Appl. Environ. Microbiol. 86 (2020), https://doi.org/10.1128/AEM.00730-20.
[34] H. Richter, B. Molitor, H. Wei, W. Chen, L. Aristilde, L.T. Angenent, Ethanol production in syngas-fermenting Clostridium ljungdahlii is controlled by thermodynamics rather than by enzyme expression, Energy Environ. Sci. 9 (2016) 2392–2399, https://doi.org/10.1039/C6EE01108J.
[35] L.A. de Lima, H. Ingelman, K. Brahmbhatt, K. Reinmets, C. Barry, A. Harris, E. Marcellin, M. Köpke, K. Valgepea, Faster Growth Enhances Low Carbon Fuel and Chemical Production Through Gas Fermentation, Front. Bioeng. Biotechnol. 10 (2022) 1–14, https://doi.org/10.3389/FBIOE.2022.879578/FULL.
[36] K. Valgepea, R. de Souza Pinto Lemgruber, T. Abdalla, S. Binos, N. Takemori, A. Takemori, Y. Tanaka, R. Tappel, M. Köpke, S.D. Simpson, L.K. Nielsen, E. Marcellin, H2 drives metabolic rearrangements in gas-fermenting Clostridium autoethanogenum, Biotechnol. Biofuels 11 (2018) 55, https://doi.org/10.1186/s13068-018-1052-9.
[37] V. Mahamkali, K. Valgepea, R. de Souza Pinto Lemgruber, M. Plan, R. Tappel, M. Köpke, S.D. Simpson, L.K. Nielsen, E. Marcellin, Redox controls metabolic robustness in the gas-fermenting acetogen Clostridium autoethanogenum, Proc. Natl. Acad. Sci. U. S. A. 117 (2020) 13168–13175, https://doi.org/10.1073/PNAS.1919531117.
[38] E. Almeida Benalcázar, Modeling the anaerobic fermentation of CO, H2 and CO2 mixtures at large and micro-scales [doctoral dissertation], Delft University of Technology, 2023.
[39] A. Grimalt-Alemany, C. Etler, K. Asimakopoulos, I.V. Skiadas, H.N. Gavala, ORP control for boosting ethanol productivity in gas fermentation systems and dynamics of redox cofactor NADH/NAD + under oxidative stress, J. CO2 Util. 50 (2021) 101589, https://doi.org/10.1016/j.jcou.2021.101589.
[40] C. Haringa, H.J. Noorman, R.F. Mudde, Lagrangian modeling of hydrodynamic–kinetic interactions in (bio)chemical reactors: Practical implementation and setup guidelines, Chem. Eng. Sci. 157 (2017) 159–168, https://doi.org/10.1016/J.CES.2016.07.031.
[41] C. Haringa, R.F. Mudde, H.J. Noorman, From industrial fermentor to CFD-guided downscaling: what have we learned? Biochem. Eng. J. 140 (2018) 57–71, https://doi.org/10.1016/j.bej.2018.09.001.
[42] D. Visser, J.J. Heijnen, Dynamic simulation and metabolic re-design of a branched pathway using linlog kinetics, Metab. Eng. 5 (2003) 164–176, https://doi.org/10.1016/S1096-7176(03)00025-9.
[43] J.J. Heijnen, Approximative kinetic formats used in metabolic network modeling, Biotechnol. Bioeng. 91 (2005) 534–545, https://doi.org/10.1002/BIT.20558.
[44] R.C.H. del Rosario, E. Mendoza, E.O. Voit, Challenges in lin-log modelling of glycolysis in Lactococcus lactis, IET Syst. Biol. 2 (2008) 136–149, https://doi.org/10.1049/IET-SYB:20070030.
[45] K. Schuchmann, V. Müller, Direct and reversible hydrogenation of CO2 to formate by a bacterial carbon dioxide reductase, Sci. (80-.) 342 (2013) 1382–1385, https://doi.org/10.1126/science.1244758.
[46] M.T. Allaart, M. Diender, D.Z. Sousa, R. Kleerebezem, Overflow metabolism at the thermodynamic limit of life: How carboxydotrophic acetogens mitigate carbon monoxide toxicity, Microb. Biotechnol. 16 (2023) 697–705, https://doi.org/10.1111/1751-7915.14212.
[47] J. Seravalli, M. Kumar, W.P. Lu, S.W. Ragsdale, Mechanism of carbon monoxide oxidation by the carbon monoxide dehydrogenase/acetyl-CoA synthase from Clostridium thermoaceticum: Kinetic characterization of the intermediates, Biochemistry 36 (1997) 11241–11251, https://doi.org/10.1021/bi970590m.
[48] X. Li, M.A. Henson, Metabolic modeling of bacterial co-culture systems predicts enhanced carbon monoxide-to-butyrate conversion compared to monoculture systems, Biochem. Eng. J. 151 (2019) 107338, https://doi.org/10.1016/j.bej.2019.107338.
[49] A.P.J. Sweere, K.C.A.M. Luyben, N.W.F. Kossen, Regime analysis and scale-down: Tools to investigate the performance of bioreactors, Enzym. Microb. Technol. 9 (1987) 386–398, https://doi.org/10.1016/0141-0229(87)90133-5.
[50] P. Hu, S.H. Bowen, R.S. Lewis, Bioresource Technology A thermodynamic analysis of electron production during syngas fermentation, Bioresour. Technol. 102 (2011) 8071–8076, https://doi.org/10.1016/j.biortech.2011.05.080.
[51] M. Hermann, A. Teleki, S. Weitz, A. Niess, A. Freund, F.R. Bengelsdorf, R. Takors, Electron availability in CO2, CO and H2 mixtures constrains flux distribution, energy management and product formation in Clostridium ljungdahlii, Microb. Biotechnol. 13 (2020) 1831–1846, https://doi.org/10.1111/1751-7915.13625.
[52] K. van't Riet, R.G.J.M. van der Lans, Mixing in Bioreactor Vessels, Compr. Biotechnol. Second Ed. 2 (2011) 63–80, https://doi.org/10.1016/B978-0-08-088504-9.00083-0.
[53] F. Oswald, I.K. Stoll, M. Zwick, S. Herbig, J. Sauer, N. Boukis, A. Neumann, Formic Acid Formation by Clostridium ljungdahlii at Elevated Pressures of Carbon Dioxide and Hydrogen, Front. Bioeng. Biotechnol. 6 (2018) 1–10, https://doi.org/10.3389/FBIOE.2018.00006.
[54] C. Kantzow, D. Weuster-Botz, Effects of hydrogen partial pressure on autotrophic growth and product formation of Acetobacterium woodii, Bioprocess Biosyst. Eng. 39 (2016) 1325–1330, https://doi.org/10.1007/S00449-016-1600-2/TABLES/1.
[55] M.P. Elisiário, W. Van Hecke, H. De Wever, H. Noorman, A.J.J. Straathof, Acetic acid, growth rate, and mass transfer govern shifts in CO metabolism of Clostridium autoethanogenum, Appl. Microbiol. Biotechnol. 107 (2023) 5329–5340, https://doi.org/10.1007/s00253-023-12670-6.
[56] E.A. Benalcázar, H. Noorman, R.M. Filho, J. Posada, A systematic approach for the processing of experimental data from anaerobic syngas fermentations, Comput. Aided Chem. Eng. 51 (2022) 1303–1308, https://doi.org/10.1016/B978-0-323-95879-0.50218-6.
[57] K. Valgepea, R. de Souza Pinto Lemgruber, K. Meaghan, R.W. Palfreyman, T. Abdalla, B.D. Heijstra, J.B. Behrendorff, R. Tappel, M. Köpke, S.D. Simpson, L. K. Nielsen, E. Marcellin, Maintenance of ATP homeostasis triggers metabolic shifts in gas-fermenting acetogens, Cell Syst. 4 (2017) 505–515.e5, https://doi.org/10.1016/j.cels.2017.04.008.
[58] J.K. Heffernan, K. Valgepea, R. de Souza Pinto Lemgruber, I. Casini, M. Plan, R. Tappel, S.D. Simpson, M. Köpke, L.K. Nielsen, E. Marcellin, Enhancing CO2-valorization using clostridium autoethanogenum for sustainable fuel and chemicals production, Front. Bioeng. Biotechnol. 8 (2020) 1–17, https://doi.org/10.3389/fbioe.2020.00204.
[59] J. Chen, J. Daniell, D. Griffin, X. Li, M.A. Henson, Experimental testing of a spatiotemporal metabolic model for carbon monoxide fermentation with Clostridium autoethanogenum, Biochem. Eng. J. 129 (2018) 64–73, https://doi.org/10.1016/j.bej.2017.10.018.
[60] M. Mohammadi, A.R. Mohamed, G.D. Najafpour, H. Younesi, M.H. Uzir, Kinetic studies on fermentative production of biofuel from synthesis gas using clostridium ljungdahlii, Sci. World J. 2014 (2014) 1–8, https://doi.org/10.1155/2014/910590.
[61] E.M. Medeiros, J.A. Posada, H. Noorman, R.M. Filho, Dynamic modeling of syngas fermentation in a continuous stirred-tank reactor: multi-response parameter estimation and process optimization, Biotechnol. Bioeng. 116 (2019) 2473–2487, https://doi.org/10.1002/bit.27108.
[62] H. Richter, M.E. Martin, L.T. Angenent, A two-stage continuous fermentation system for conversion of syngas into ethanol, Energies 6 (2013) 3987–4000, https://doi.org/10.3390/en6083987.
[63] S. Schulz, B. Molitor, L.T. Angenent, Acetate augmentation boosts the ethanol production rate and specificity by Clostridium ljungdahlii during gas fermentation with pure carbon monoxide, Bioresour. Technol. 369 (2023) 128387, https://doi.org/10.1016/j.biortech.2022.128387.
[64] H. Xu, C. Liang, X. Chen, J. Xu, Q. Yu, Y. Zhang, Z. Yuan, Impact of exogenous acetate on ethanol formation and gene transcription for key enzymes in Clostridium autoethanogenum grown on CO, Biochem. Eng. J. 155 (2020) 107470, https://doi.org/10.1016/j.bej.2019.107470.
[65] J. Bertsch, V. Müller, Bioenergetic constraints for conversion of syngas to biofuels in acetogenic bacteria, Biotechnol. Biofuels 8 (1) (2015) 12, https://doi.org/10.1186/s13068-015-0393-x.
[66] A.E. Benalcázar, H. Noorman, R. Maciel Filho, J.A. Posada, Modeling ethanol production through gas fermentation: a biothermodynamics and mass transfer-based hybrid model for microbial growth in a large-scale bubble column bioreactor, Biotechnol. Biofuels 13 (1) (2020) 19, https://doi.org/10.1186/s13068-020-01695-y.
[67] B. Niebel, S. Leupold, M. Heinemann, An upper limit on Gibbs energy dissipation governs cellular metabolism, Nat. Metab. 1 (2019) 125–132, https://doi.org/10.1038/s42255-018-0006-7.
[68] A.G. Fredrickson, G. Stephanopoulos, Microbial competition, Sci. (80-.) 213 (1981) 972–979, https://doi.org/10.1126/science.7268409.
[69] E. Biegel, S. Schmidt, J.M. González, V. Müller, Biochemistry, evolution and physiological function of the Rnf complex, a novel ion-motive electron transport complex in prokaryotes, Cell. Mol. Life Sci. 68 (2011) 613–634, https://doi.org/10.1007/s00018-010-0555-8.
[70] S. Wang, H. Huang, H.H. Kahnt, A.P. Mueller, M. Köpke, R.K. Thauer, NADP-Specific electron-bifurcating [FeFe]-hydrogenase in a functional complex with formate dehydrogenase in clostridium autoethanogenum grown on CO, J. Bacteriol. 195 (2013) 4373–4386, https://doi.org/10.1128/JB.00678-13/SUPPL_FILE/ZJB9990928O3SO1.PDF.
[71] A. Panneerselvam, M.R. Wilkins, M.J.M. DeLorme, H.K. Atiyeh, R.L. Huhnke, Effects of various reducing agents on syngas fermentation by clostridium ragsdalei, Biol. Eng. 2 (2010) 135–144, https://doi.org/10.13031/2013.34831.
[72] J. Lo, D.G. Olson, S.J.L. Murphy, L. Tian, S. Hon, A. Lanahan, A.M. Guss, L.R. Lynd, Engineering electron metabolism to increase ethanol production in Clostridium thermocellum, Metab. Eng. 39 (2017) 71–79, https://doi.org/10.1016/j.ymben.2016.10.018.

[73] A. Mayer, T. Schädler, S. Trunz, T. Stelzer, D. Weuster-Botz, Carbon monoxide conversion with Clostridium aceticum, Biotechnol. Bioeng. 115 (2018) 2740–2750, https://doi.org/10.1002/bit.26808.
[74] M. Mann, K. Miebach, J. Büchs, Online measurement of dissolved carbon monoxide concentrations reveals critical operating conditions in gas fermentation experiments, Biotechnol. Bioeng. 118 (2021) 253–264, https://doi.org/10.1002/BIT.27567.
[75] E. Biegel, V. Müller, Bacterial Na+-translocating ferredoxin: NAD+ oxidoreductase, Proc. Natl. Acad. Sci. U. S. A. 107 (2010) 18138–18142, https://doi.org/10.1073/pnas.1010318107.
[76] L. Perec, A.I. Krasna, D. Rittenberg, The inhibition of hydrogenase by carbon monoxide and the reversal of this inhibition by light, Biochemistry 1 (1962) 270–275, https://doi.org/10.1021/bi00908a013.
[77] A.I. Krasna, Hydrogenase: properties and applications, Enzym. Microb. Technol. 1 (1979) 165–172, https://doi.org/10.1016/0141-0229(79)90023-1.
[78] D. Lao-Martil, J.P.J. Schmitz, B. Teusink, N.A.W. van Riel, Elucidating yeast glycolytic dynamics at steady state growth and glucose pulses through kinetic metabolic modeling, Metab. Eng. 77 (2023) 128–142, https://doi.org/10.1016/j.ymben.2023.03.005.
[79] W. Tang, Struct. Kinet. Model. Ration. Scale- Des. Optim. Ind. Ferment. (2022), https://doi.org/10.4233/uuid:cfe84a26-e30f-430d-8ad1-3d503e780e36.